ORIGINAL ARTICLE

An investigation on microstructural features and bonding strength of magnesium-based multifunctional laminated composite developed by friction stir additive manufacturing

Amit Rai Dixit[1] · Ashish Kumar Srivastava[2] · Suryank Dwivedi[1] · Akash Nag[3] · Sergej Hloch[3]

Abstract

Recently, the demand for lightweight multilayered parts in electronics and biomedical fields has been accelerated and shown great interest in understanding the combined effect of multilayered materials. However, these industries are still facing the challenge of developing dissimilar multilayered materials that can be suitable for biomedical applications. In this context, magnesium emerges as a promising biocompatible material used for several biomedical applications. However, the issues related to joining magnesium alloys with other similar materials still need to be solved. Moreover, friction stir additive manufacturing (FSAM) occupies a niche domain for developing or joining biocompatible materials such as magnesium alloys with low weight and high strength. Therefore, the present work highlights the development of a multipurpose three-layered multifunctional laminated composite plate of magnesium-based AZ31B–Zn–Al 1100 through the FSAM route. Microstructural and morphological examinations were carried out by light microscopy and FESEM equipped with EDS analysis and line mapping. Moreover, the grain refinement at the interfaces during the FSAM was also addressed using the electron backscattered diffraction (EBSD) study. Further, investigation on mechanical properties such as tensile test with fractography analysis and microhardness variation at the cross-section of the built-up section has been investigated. Furthermore, the corrosion and tribological analysis was also performed, and a 3D profilometer was used to visualize the corroded and worn-out surfaces. The microstructural results revealed that the average grain size of 6.29 µm at interface AZ31B–Zn and 1.21 µm at interface Zn–Al 1100 occurred, improving the bonding strength and overall properties. The tensile strength has occurred as 171.5 MPa at 15.5% elongation, whereas maximum microhardness is reported as 105 HV at the interface of AZ31B–Zn and 84.6 HV at the interface of Zn–Al 1100. The corrosion rate was calculated as 0.00244 mm/day, and the average coefficients of friction (COF) for both the interfaces, such as AZ31B–Zn and Zn–Al 1100, are 0.309 and 0.212, respectively.

Keywords Friction stir additive manufacturing · Laminated composite · AZ31B · EBSD · Tensile strength · Corrosion test · Tribological performance

✉ Sergej Hloch
sergej.hloch@vsb.cz

1   Indian Institute of Technology (ISM), Dhanbad, Jharkhand, 826004, India

2   G L Bajaj Institute of Technology and Management, Greater Noida, (UP), 201308, India

3   Faculty of Mechanical Engineering, VŠB - Technical University of Ostrava, 17. listopadu 2172/15, 70800 Ostrava-Poruba, Czech Republic

1 Introduction

The electronic and medical industries demanded sophisticated and lightweight multilayered materials which can be suitable for a wide range of operating temperatures with improved performance. The prime requirement for these materials is properties like high strength-to-weight ratio, electrical and thermal conductivities, improved tribological properties, and anticorrosion behavior. While dealing with biocompatible materials like magnesium alloys, whose modulus of elasticity and density align with the human bone, have major demand to make bio-implants and artificial socket joints [1], some studies show that due to the wear of

the implant, incompatible ions are released into the human's physiological environment, causing adverse reactions [2]. Therefore, magnesium-based laminated composites have gained more focus due to their excellent mechanical and tribological properties [3, 4]. However, due to poor formability and less symmetrical hexagonal structure, magnesium alloys' processing (plastic deformation) is complex [5]. In the revolutionary appraisal of Industry 4.0, additive manufacturing (AM) is rapidly becoming a famous method used to develop physical components of magnesium-based components. Still, it has challenges associated with the defects and degradation of mechanical properties [6]. The different methods of AM, like 3D screen printing [7], direct energy deposition [8], powder bed fusion [9], metal jetting [10], and sheet metal lamination, are most famous for processing the magnesium and other metallic materials and alloys due to its excellency in producing complex parts in minimum time and negligible material wastage [11].

Friction stir additive manufacturing (FSAM) is a kind of sheet metal lamination method of the solid-state additive manufacturing method, which utilizes the mechanism of friction stir welding (FSW) [12–14]. FSW was first applied by The Welding Institute (TWI) in 1991 to weld the metallic layers by means of frictional heat and applied pressure [15]. The process comprises a cylindrical rotating tool of hard material having a specially designed tool pin with sufficient shoulder diameter subjected to an axial applied pressure on it, as shown in Fig. 1(a). The tool pin is inserted into the top of the base plate, which is tightly fixed into a fixture. The tool is allowed to move in the traverse direction with a rational speed along a predefined path which induces frictional heat. Due to the effect of frictional heat, the material undergoes severe plastic deformation above the recrystallization temperature and joins or processes the adjacent sides of the weld plates. Since FSW is a solid-state processing with negligible gas emissions, the technology is further modified as FSAM, which can build up the layer-by-layer 3D physical component of similar or dissimilar material, as shown in Fig. 1(b and c) [15, 16]. Therefore, the combination of different metallic layers can also be produced by FSAM with altered properties. Compared to friction stir lap welding (FSLW), FSAM is designed to process the complete overlapped area of thin plates with a specially designed array or sequence of the path of FSW experiments by making a series of stir zone (SZ) (Fig. 1(b and c)) [17, 18]. Hence, FSAM has also been termed as a tailored version of the FSLW [19].

Standard Mg alloy implants release hydrogen gas which fails the implant by detaching the body cell from the bone [20–22]. The FSAM can easily overcome these issues by adding biocompatible layers of magnesium alloys with other similar materials like aluminum, zinc, etc., which enhances the desired properties of magnesium alloy but does not come directly in contact with the
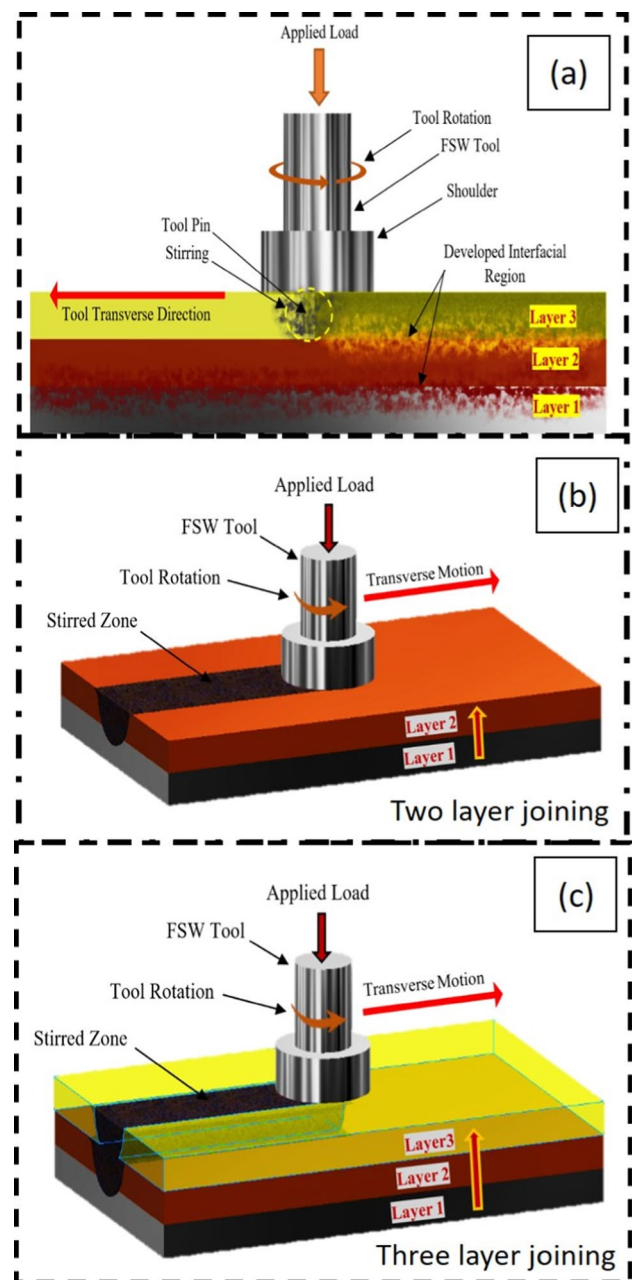

Fig. 1 **a** Schematic arrangement of friction stir additive manufacturing, **b** two-layer joining, and **c** three-layer joining

human body parts [21]. Further, the severe plastic deformation capability of FSAM also breaks the less hexagonal structure into refined equiaxed grains with a large number of grain boundaries which is one of the challenging tasks with other similar manufacturing techniques due to the low formability of magnesium alloys [22, 23]. Several authors have tried to overcome the issues related to material, such as Palanivel et al. [24] developed four layered composites with WE43 by FSAM method, each of 1.7 mm with a total height of 5.6 mm. Lap welding with the

layer-by-layer technique for developing the part was used. In the processed part, defects like hooking, cavity, and cracks due to differences in the microstructural feature were found. The results suggested maintaining sufficient frictional heat to overcome these defects. Ho et al. [25, 26] developed a stacked composite of AZ31B magnesium and hydroxyapatite through the FSAM method. The developed composite overcomes the challenging issues of corrosion. Also, the apatite formation and body cell adhesion over the Mg alloy surface improved. The outcomes also advocated the improved corrosion behavior of AZ31B through in-vitro tests. Similar to the FSAM process, additive friction stir deposition (AFSD) is also famous for the deposition of different materials over a plate substrate and for repairing or overcoming the defects that arise during the FSP operation. FSAM has tracing importance in the field of biomaterials, which is also suggested by Staiger MP et al. [21]. This method also fulfills the requirements of biodegradable materials with low weight and high strength. Martin, L.P., et al. [27] repair the Al6061-T6 machined groove surface by depositing the additive layer, which overcomes the surface defects like cracks and voids. They observed that the AFSD can improve the surface efficiently, which leads to improved mechanical properties like tensile strength.

Based on the archival of the literature, it is found that FSAM can also be suitable for layer-by-layer joining of dissimilar materials if suitable process parameters can be selected. In this paper, an attempt is made to develop a 3D laminated composite of dissimilar materials for multipurpose industrial and medical applications. Confirming the advantages of FSAM and its capability to process biocompatible materials like magnesium, the present investigation deals with the magnesium-based laminated 3D composite plate of AZ31B–Zn–Al 1100 developed by layer-by-layer joining through FSAM. The study shows the effect of process parameters on developing a three-layer laminated composite and discusses the defects associated with a different range of process parameters. The microstructural and morphological characteristics of interfacial layers between the adjacent layers are validated through light microscopy and FESEM images with EDS elemental analysis and line mapping images. EBSD (electron backscattered diffraction) analysis is also conducted to discuss the crystallographic planes and grain structures at both interfaces. Further, to evaluate the mechanical properties, the tensile test with fractographic FESEM images and microhardness throughout the cross-section of the built-up section is discussed in detail. Corrosion and tribological studies are also conducted and discussed with their findings through the 3D surface profile of corroded layers and wear tracks, respectively.

2 Experimental procedure

In the present investigation, three commercially available and commonly used dissimilar materials, namely, AZ31B magnesium alloy (melting point: 605 °C), zinc (99.9% pure zinc, melting point: 415 °C), and aluminum Al 1100 (99.0% pure aluminum, melting point: 650 °C), are considered to develop the laminated composite 3D plate through layer-by-layer FSAM. AZ31B plate (size 100 mm × 100 mm × 5 mm) is used as a base of the 3D composite plate covered by Zn plate (size 100 mm × 100 mm × 3 mm) and Al 1100 (size 100 mm × 100 mm × 2 mm). It is to be noted that Zn has a low melting temperature compared to AZ31B and Al 1100; therefore, Zn is used as an intermediate binder between the magnesium and aluminum plate. A semiautomatic Ace Macromatic Group (AMS) CNC milling machine is used to perform the FSAM process with an in-house design fixture, as shown in Fig. 2(a). In order to perform the FSAM operation, a square probe tool of 4 mm of each dimension with an 18 mm shoulder diameter is used in this study (Fig. 2 (d)). The tool was rotated at a constant rotational speed of 3000 rpm, feed rate of 25 mm/min with 0° tilt angle, and dwelling time of 20 s. Moreover, the process parameter selection is based on the pilot run and the author's previously published work related to the statistical data on the experiments. These process parameters are optimized sets of input variables required to justify all three selected materials. The FSAM of two-layer joining (AZ31B–Zn) and third-layer joining (Zn–Al 1100) is shown in Fig. 2 (b and c) with their temperature profile shown in Fig. 2 (e and f) through a digital thermal camera to monitor the temperature variation throughout the process continually. The final laminated 3D composite plate and its cross-section view are shown in Fig. 2 (g and h).

The microstructural and mechanical properties of the developed composite plate are evaluated. The specimen for the microstructural study is prepared as per ASTM-E3 standard, followed by polishing with diamond paste and cleaning through ultrasonic cleanser to remove oxide layers. The sample was further electropolished at 16 V for 20 s in the solution of isopropanol (80%) and perchloric acid (20%) to conduct the grain refinement study at the interface and within the stir zone through electron backscattered diffraction (EBSD). The light microscopy was performed by an inverted optical microscope (Leica-DMI3000M). Further, FESEM with EDS elemental validation was studied through Carl Zeiss-SIGMA at an acceleration voltage of 15 kV with an acquisition time of 60.4 s to investigate the microstructural features at both material interfaces. To conduct tensile testing, the specimen was taken from the stir zone of the built-up section
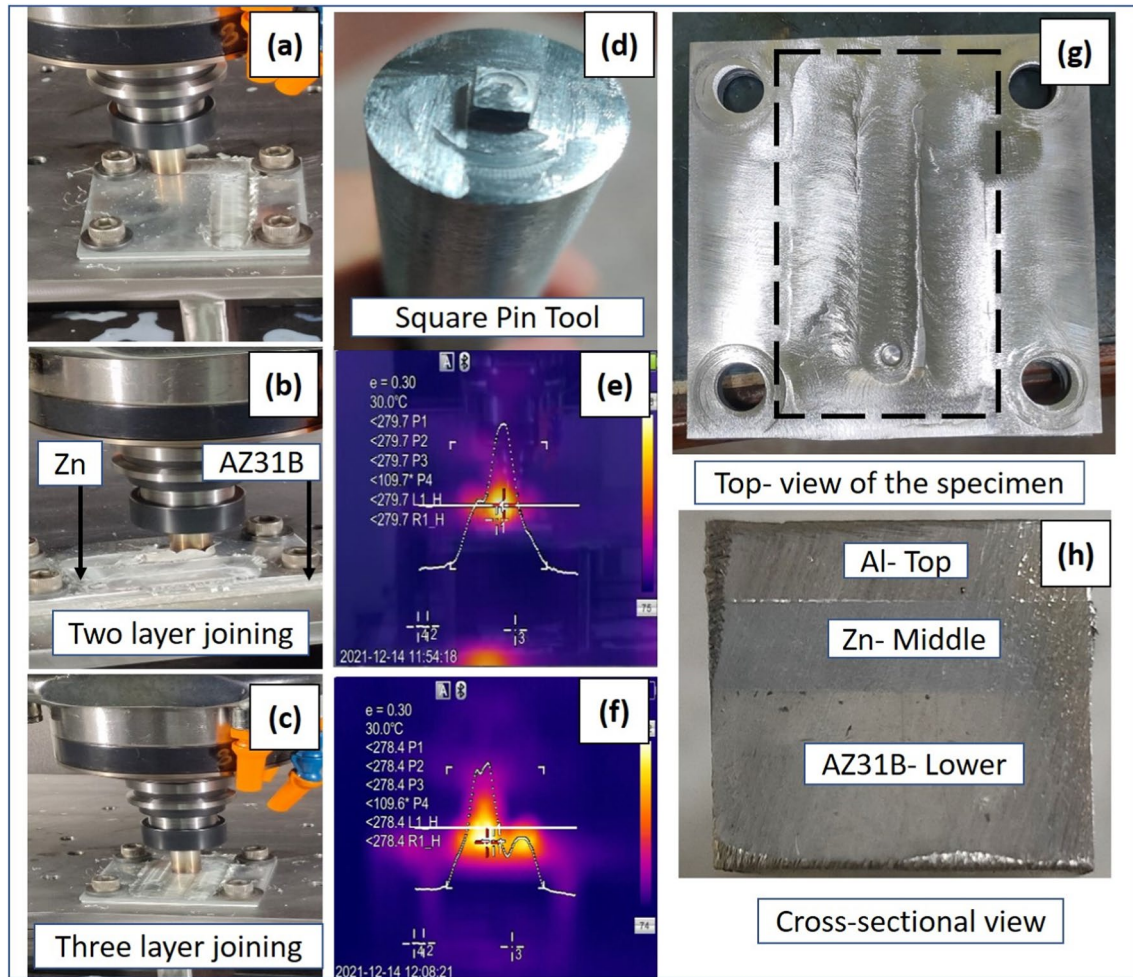
Fig. 2 Friction stir additive manufacturing process of AZ31B–Zn–Al 1100 laminated 3D composite plate

according to the ASTM-E8 standard. The unprocessed (base material) AZ31B, Zn, and Al 1100 specimens are also prepared separately to test and compare tensile strength results with percent elongation. The tensile test was conducted through a biaxial planner tensile testing machine (make: Instron at IIT-ISM Dhanbad, India) at a 1 mm/min strain rate. As a result, the stress-strain curve, neck formation, and fractured specimen are discussed in detail to validate the results. The fractography of the fractured specimen through FSESEM images is investigated to support the understanding of the tensile behavior of the laminated 3D composite. Further, the microhardness variation throughout the cross-section of the built-up section of the 3D composite plate was investigated through Vickers's hardness testing machine (model: ECONOMET VH-1MD, make: Chennai Metco, India) at a load of 100 g for 10 s. The microhardness test was conducted from the bottom of AZ31B (0 point) to the top of the Al 1100 (10 mm) with 20 readings of 0.5 mm step size. Furthermore, the corrosion analysis of the FSAM sample was performed

through the weight loss method. The sample was mechanically polished and ultrasonically cleaned in the acetone and DI bathtub to remove the oxide layers. The prepared sample was placed in the 0.9 NaCl salt solution for 7 days. Before starting and at the end of the corrosion study, the initial and final weights were measured. Further, the corrosion rate was calculated using Eq. (1) [28].

$$Corrosion\ rate\ (CR) = 87.6 \times \frac{(\Delta W)}{(\rho AT)}\ \text{mm/year} \qquad (1)$$

ΔW represents the change in weight (mg), ρ denotes the sample density (g/cm^3), A is the exposed surface area (cm^2), and T is the total test duration (hour),

3D surface profiles of the prepared sample were taken before and after the corrosion test by a 3D optical profilometer (model: New View 9000, make: Zygo, USA) to discuss the corrosion effect on different layers. Moreover, laminated composite prepared by friction stir additive manufacturing comprising Al–Zn–Mg alloy has different tribological

behavior. Therefore, to understand the tribological performance of the composite, dry tribological wear analysis was performed at a reciprocating ball-on-plate universal tribometer (Model: MFT 5000, Make: Rtec, USA). The dry sliding friction and wear test was performed at the interface of Al–Zn and Zn–Mg and compared with base materials such as Al, Zn, and Mg, respectively. A stainless steel 316 ball of 6 mm diameter was used as a counter body part during the test. The friction and wear test was performed at a 10 N load with a sliding frequency of 5 Hz for a duration of 300 s. The test was done at a room temperature of 25 ± 1 °C and relative humidity (RH) was set to 45 ± 2 RH. The friction and wear test was repeated thrice, and the average values were taken for further analysis. At last, the tribological performance of the laminated composite was evaluated in terms of coefficient of friction (COF), variation in COF vs. time, wear depth, and wear width. After the friction and wear test,

the samples were ultrasonically cleaned in acetone and dried in the open air. Furthermore, to understand the wear mode, profiles of wear tracks were captured using the non-contact 3D optical profilometer (model: New View 9000, make: Zygo, USA). The 3D surface profiles and wear depth and width values of worn-out samples were obtained and further analyzed to understand the wear mechanism.

3 Result and discussion

The findings first discuss the effect of process parameters on the development of the three-layered laminated composite. During the laminated process of AZ31B–Zn–Al1100, a set of process parameters are required, which can be suitable for each layer lamination. Several pilot experiments were conducted to select the optimized set of process parameters.
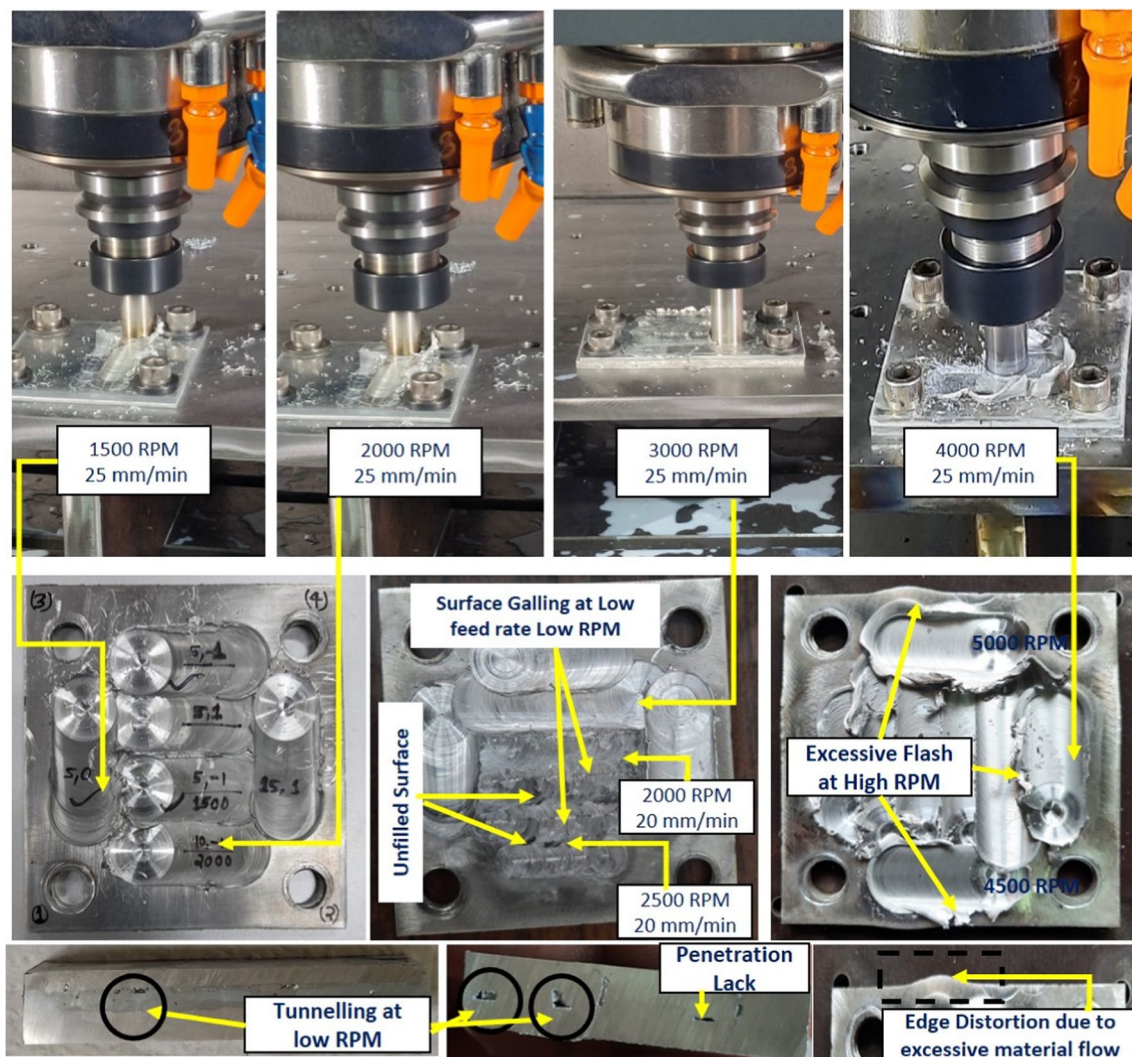

Fig. 3 Effect of process parameters and defects arises during the experimentation

Rotational speed and feed rate were taken in the range of 1500 to 5000 rpm with a feed rate of 20 to 25 mm/min while keeping a 0° tilt angle. Figure 3 shows the various pilot operations with the effect of process parameters and defects arises during the experimentation. From Fig. 3, it can be noticed that at low speeds (1500, 2000, and 2500 rpm), the formation of tunneling, lack of diffusion, and tool pin penetration were high. It is because, at low rpm, the processing heat is insufficient, which hinders material flow and extrusion, leading to poor diffusion (poor plastic deformation) and forming tunnels and surface galling. Further, increasing the RPM (4000, 4500, and 5000) or decreasing the feed rate (20 mm/min) leads to excessive flash over the processed surface. Other researchers also observed similar findings in the past [29, 30]. The excessive heat generation can melt the intermediate Zn layer, and its molten will flow out from the corners during the second run while joining AZ31B. The high frictional heat supports smooth operation. However, it greatly reduces the overall thickness of the composite plate under the action of axial force and excessive plastic deformation [31]. The edge distortion can also be occurred due to excessive plastic deformation of low-melting material like zinc.

Figure 4 shows the macroscopic cross-sectional view of the physically developed AZ31B–Zn–Al 1100 laminated composite specimen. The macro-image of the specimen shows the sound joining of the three different plates one upon another. Further, to visualize the zoom view, microscopic images were taken from 5 sites of the samples, three from the joining materials and two from the interfacial sites formed while joining these three materials. The Mg–Zn interface clearly shows the uniform intermixing of both the materials at the interface leading to stronger intermetallic bonds. Also, the same feature was observed with the Al–Zn interface, where a clear boundary showed the different material structures. However, the Mg–Zn interface mixing was enhanced due to repetitive loading and propagation of induced heat at the interface twice during the fabrication of the whole specimen.

Figure 5 (a) shows the FESEM images and EDS spectrum of the AZ31B–Zn–Al 1100 laminated composite interfaces. The variation in the contrast of the microscopic interface image revealed the presence of one material in another, leading to the non-homogeneous distribution of the grains. However, some impurities were observed throughout the cross-section in the FESEM image of the 3-layer specimen site. FESEM images also show the apparent mixing of the materials at the interfacial zones. Figure 5 (b, c) shows the elemental line mapping of EDS analysis, which reveals the presence of the joining materials at both the formed interfaces. In interface-1 (Fig. 5b), Mg and Zn were present in 41% and 24.88% by weight, respectively, depicting the presence of Zn in the Mg material. Also, at interface-2 (Fig. 5c),
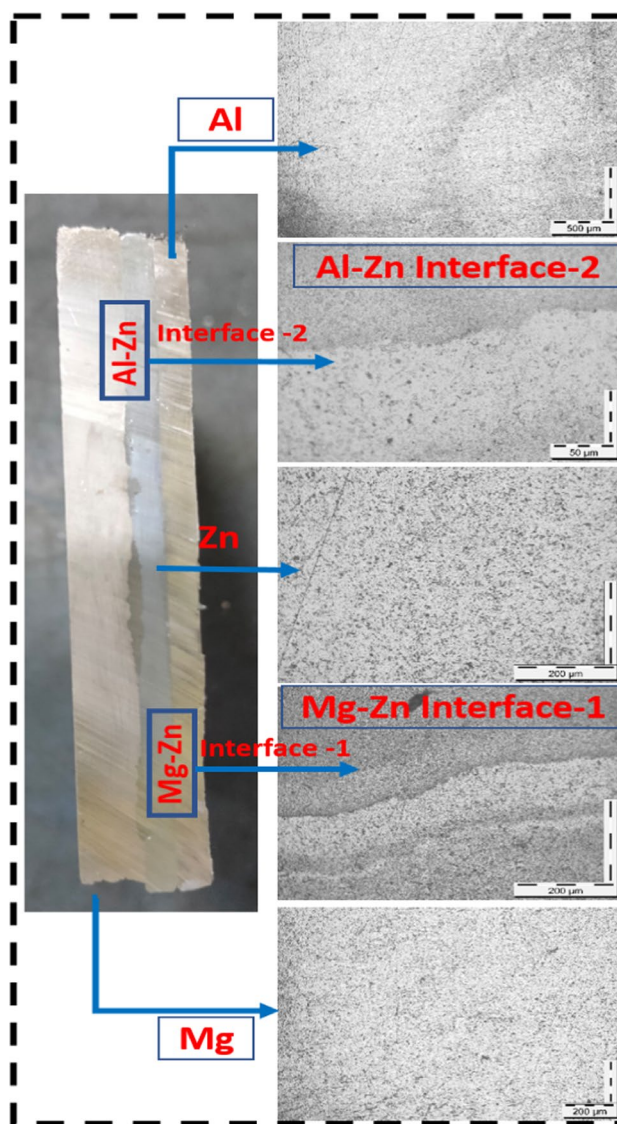

Fig. 4 Physical specimen and light microscopy images of layers of AZ31B–Zn–Al 1100 laminated composite

Al and Zn were present in 46.76% and 23.36% by weight, respectively. Zn works as a binding material between Mg and Al layers, enhancing the overall property of the additively manufactured composite.

FSAM has the ability of improved bonding strength due to the exquisiteness of its grain refinement and microstructural modification technique at the interface of similar or dissimilar materials. To support the notion, an EBSD test has been conducted on both interfaces at the SZ area (see Fig. 6a and b). The reason behind the selection of the EBSD zone at SZ is to discuss the minimum and average grain size, structure, and orientation of grains during intermixing of Al–Zn and Zn–Mg alloys. The pole figures at different crystallographic planes show the refined grains' orientation in the interfacial site between the two material layers. At
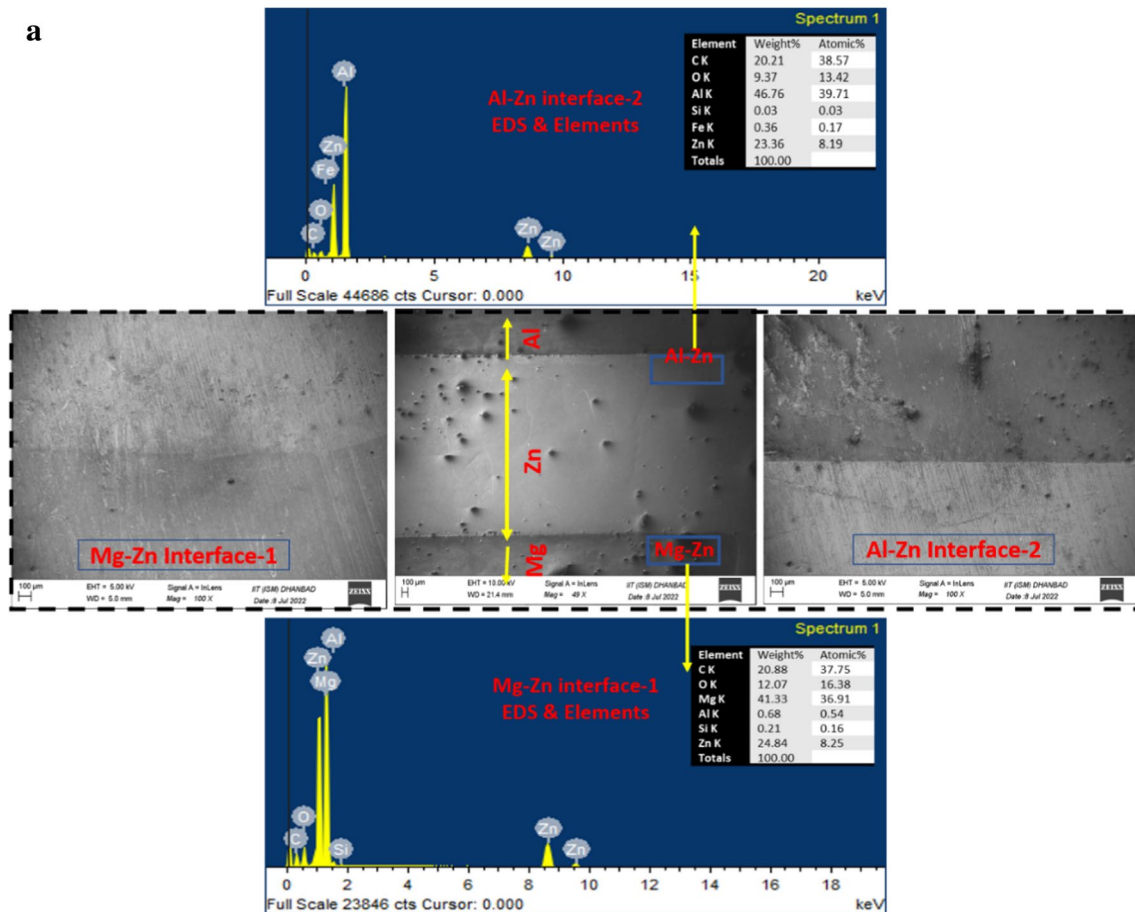
Fig. 5 **a** FESEM images and EDS spectrum of interface layers of AZ31B–Zn–Al 1100 laminated composite **b** Line mapping of AZ31B–Zn interface-1 **c** Line mapping of Zn–Al1100 interface-2

interface-1, the nature of orientation of grains toward the normal direction at <111> crystallographic plane is a little higher than in other directions. However, it can be concluded that the Mg–Zn grains do not orient in any specific direction during mixing via friction stir processing. However, at interface-2, the significant orientation of the grains toward the rolling direction is observed at <001> crystallographic plane. Under elevated temperatures, the grains undergo continuous, discontinuous, and geometric dynamic recrystallization during the plastic deformation. This phenomenon occurred during the FSAM and led to the formation of high-angle grain boundaries at the interfacial sites. Also, the high temperature associated with plastic deformation enhances the material's dynamic recrystallization and grain refinement during the process [19, 32, 33].

The average grain diameter size obtained at interface-1 was calculated to be 6.29 μm. Also, the microstructural grain distribution image represents the presence of both Mg and Zn grains at the interface. Refinement of the grains leads to enhanced properties of the fabricated composite specimen rather than individual material. The presence of HAGBs was

calculated to be 71.8%, compared to 19.2% LAGBs representing the formation of special boundaries such as twins. Also, the grain fraction shows a specific range of lower misorientation boundaries is highest for LAGBs. For interface-2, the average grain size was 1.21 μm, much smaller than interface-1. The larger grain sizes can be due to the geometrical coalescence of grains in a specific situation where two or more grains merge to form a more prominent grain under the thermal effect during FSAM. With the increased number of cycles, the probability of obtaining a more prominent grain at the lower layers increases, which may be one of the reasons for the increased grain size diameter at interface 2. HAGBs calculated at interface-2 was 64.6%, a typical fraction for grains undergoing the FSAM process. Similar to interface-1, a significant fraction of grains with a specific range of lower misorientation angles is 21.5%.

Figure 7 (a) shows the ASTM E8 standard tensile specimen, neck formation, and fractured view during the testing, and Fig. 7 (b) shows the engineering stress-strain curve of built-up AZ31B–Zn–Al 1100 layers and pure material specimens. Each base material is also tested
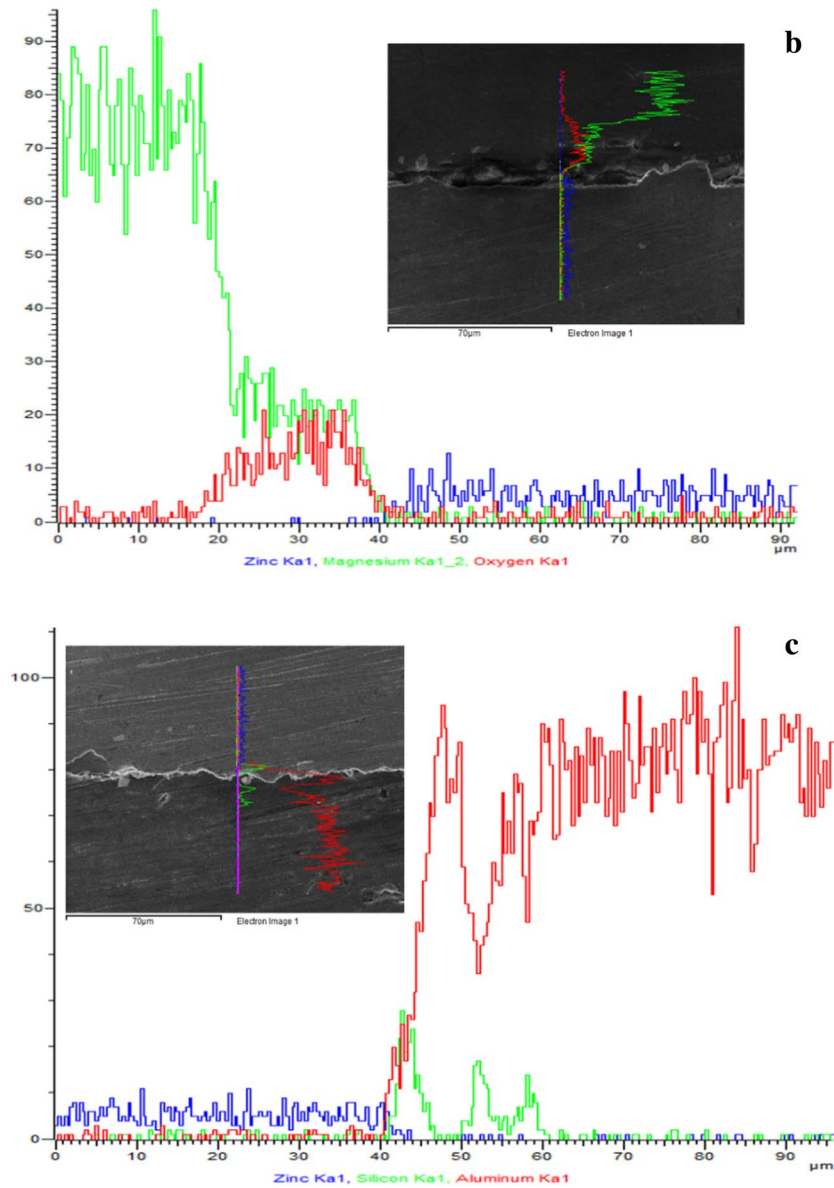
Fig. 5 (continued)

separately to evaluate its individual tensile properties for comparison purposes. It is revealed from the result obtained that the individual tensile strengths of Al 1100, Zn, and AZ31B are 93 MPa, 260.7 MPa, and 249.5 MPa, respectively. The percentage elongation corresponding to the same parent materials is 1.9%, 9%, and 10.4%, respectively. The tensile strength of the built-up specimen of AZ31B–Zn–Al 1100 layer is reported as 171.5 MPa at 15.5% elongation. It is to be noted that all three layers have different values of tensile strength and percentage elongation. Both interfaces undergo severe plastic deformation while joining these three layers through the friction stir processing, leading to the dynamic recrystallization and grain recovery phenomenon [34, 35].

Figure 8 shows the microhardness variation throughout the cross-section along the built-up direction. The microhardness values of the base materials AZ31B, Zn, and Al 1100 are obtained as 84 HV, 66 HV, and 38 HV, respectively. In comparison, the microhardness variation is observed while these layers are additively joined. The Vickers hardness of 105 HV is obtained at the first interface of AZ31B–Zn and 84.6 HV at the second interface of Zn–Al 1100. The micro-hardness graph shows the abrupt change in the microhardness values in the stir zone area of the first and second interfaces. A decreasing trend in microhardness values was reported in the thermomechanical affected zone (TMAZ), heat affected zone (HAZ), and base material (BM), which is in line with the previous study [36, 37]. Overall,

Fig. 6 **a.** EBSD and grain refinement study at the interface of AZ31B–Zn interface-1 **b** EBSD and grain refinement study at the interface of Al 1100–Zn interface-2
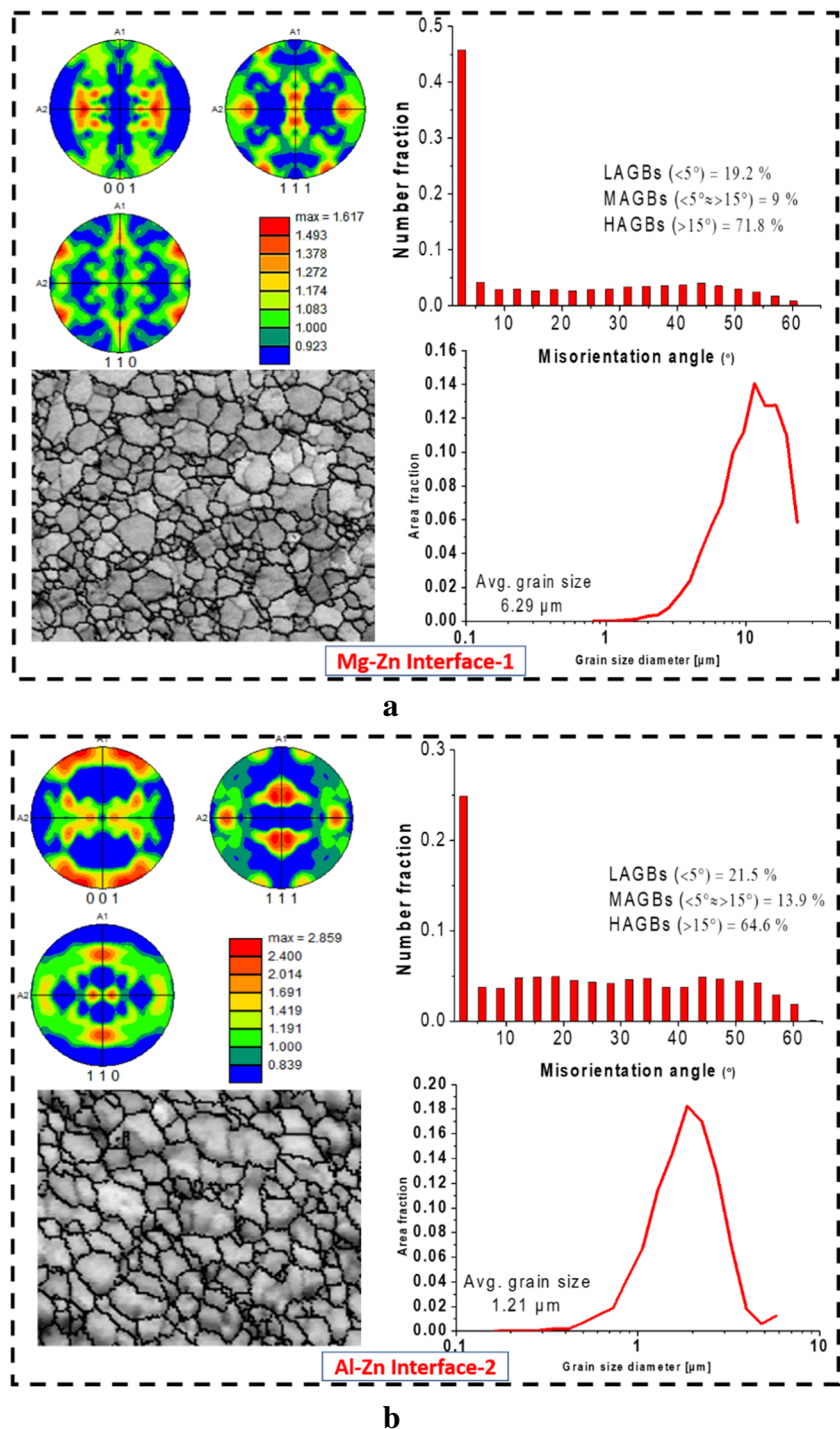
the microhardness value improved in comparison with their base material values. The improved tensile properties and microhardness are attributed to the grain refinement, microstructural modification, and increased number of grain boundaries in the stir zone.

When the first two layers, AZ31B and Zn, join together with the help of frictional heating and severe plastic deformation, it may be possible that defects such as tunnels, blow

holes, cavities, and micro-pores can be formed at the interface of the two layers. However, during the third layer processing of Al 1100 over the Zn layer through the frictional heat, the process has the advantage of joining the second interface and having sufficient heat to modify and overcome the defects that arise during the first processing [38]. It is because the plastic deformation of the Zn plate is higher than AZ31B alloy due to the low melting temperature of Zn.
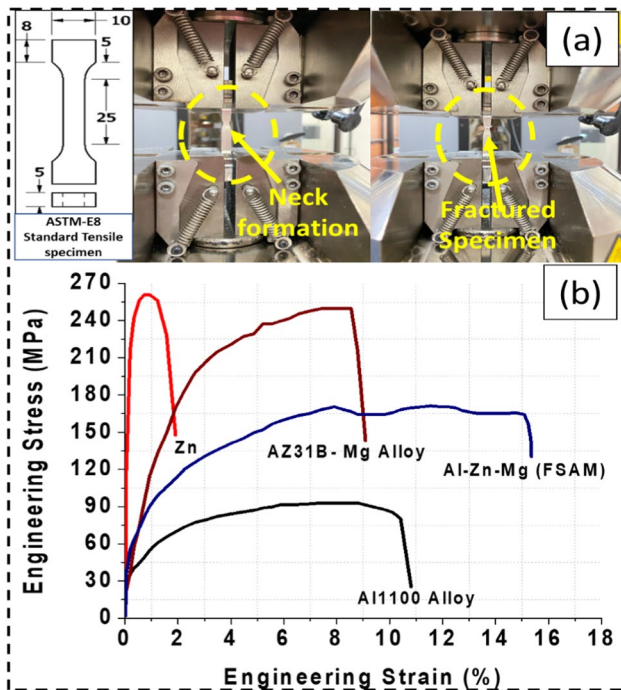
Fig. 7 **a** ASTM E8 standard tensile specimen, neck formation, fractured view during the testing, and **b** engineering stress-strain curve of built-up AZ31B–Zn–Al 1100 laminated composite and pure material specimens
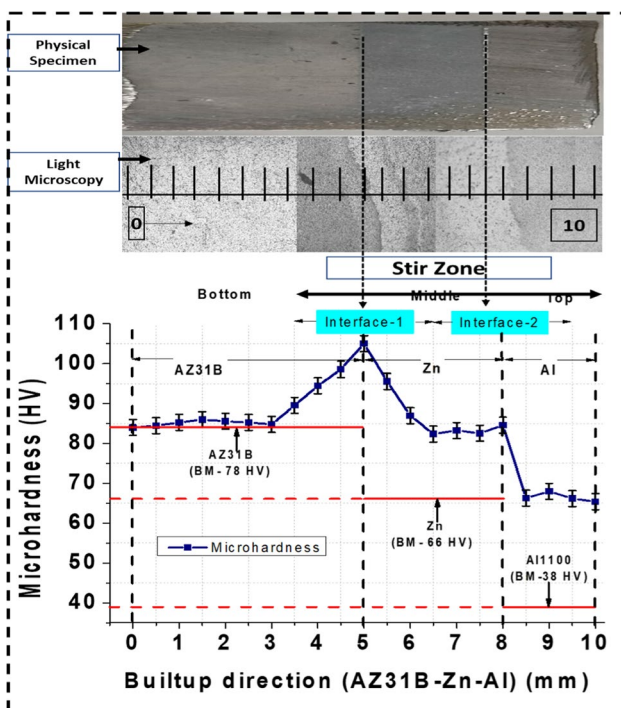

Fig. 8 Microhardness test results of AZ31B–Zn–Al 1100 laminated composite and pure material specimens

Therefore, heat is transferred throughout the Zn layer up to the first interface while joining the second interface. At the high friction heat (approx. 90% of the melting temperature of Zn), the fluidity of Zn is sufficient to fill the previously occurred defects like cavities, tunnels, and micro-holes and reduces the possible defects significantly at the interfaces. Similar findings were reported by other authors also [27, 39]. This is also the reason behind the increased microhardness of the Zn layer compared to its BM value. Therefore, Zn plays a vital role in healing material to improve the bonding between AZ31B and Al 1100. With the grain refinement technique of FSP and reduced defects due to the Zn layer at interface regions, the strengthening mechanism improves, which is associated with the strong bonding between the AZ31B–Zn–Al 1100 additive layers. However, beyond the interface layers toward the top and bottom sides of the specimen, the specimen experiences the tensile strength of base material which is relatively lower than the interface layer because of the non-processed zone. Therefore, the initial crack formation will start from the top or bottom side across the cross-section. The neck formation during the tensile testing shows that the composite layers are strongly bonded to each other and depend on the bonding strength of the composite layer [40]. The cross-section of each layer is reduced at the same location with the same crack propagation. The fractured view shows the standard fracture morphology of the tensile specimen. Each layer is broken through the same crack propagation. Figure 9 shows the FESEM images of the fractured specimen during tensile testing. The images were taken in the individual region of each matrix alloy and at the interface regions. The overall morphological examination shows ductile failure behavior. The fractured images of the interface region show the ploughing action. The morphological aspects at both sides of the interface regions are different in nature, which can be observed from the images. The fractured surface shows ductile striations and tear ridges. However, flat shear mixed with brittle fracture can also be seen in fewer regions. The fractured specimen is also associated with the dimple nature of failure at the interface region. It is attributed to the fact that at the interface region of two distinct materials, the friction stir processing creates severe plastic deformation and breaks the matrix material's larger grains into smaller grains. These equiaxed oriented grains and refined grains from the advancing to the retreating side are also confirmed by the EBSD analysis shown in Fig. 6 (a, b). These equiaxed refined grain structures improve the bonding strength at the interface. During fracture, the force acts against the bonding strength and easily fractures the weak zone of the interface. This leads to severe ductile striation and creates dimples on the fractured surface. The other observations, such as tear ridges, micro-pores, large pores, micro-cracks, and shear bonds of both long and short lengths, can be seen in the FESEM images of the different

Fig. 9 Fractographic analysis of the tensile fractured specimen
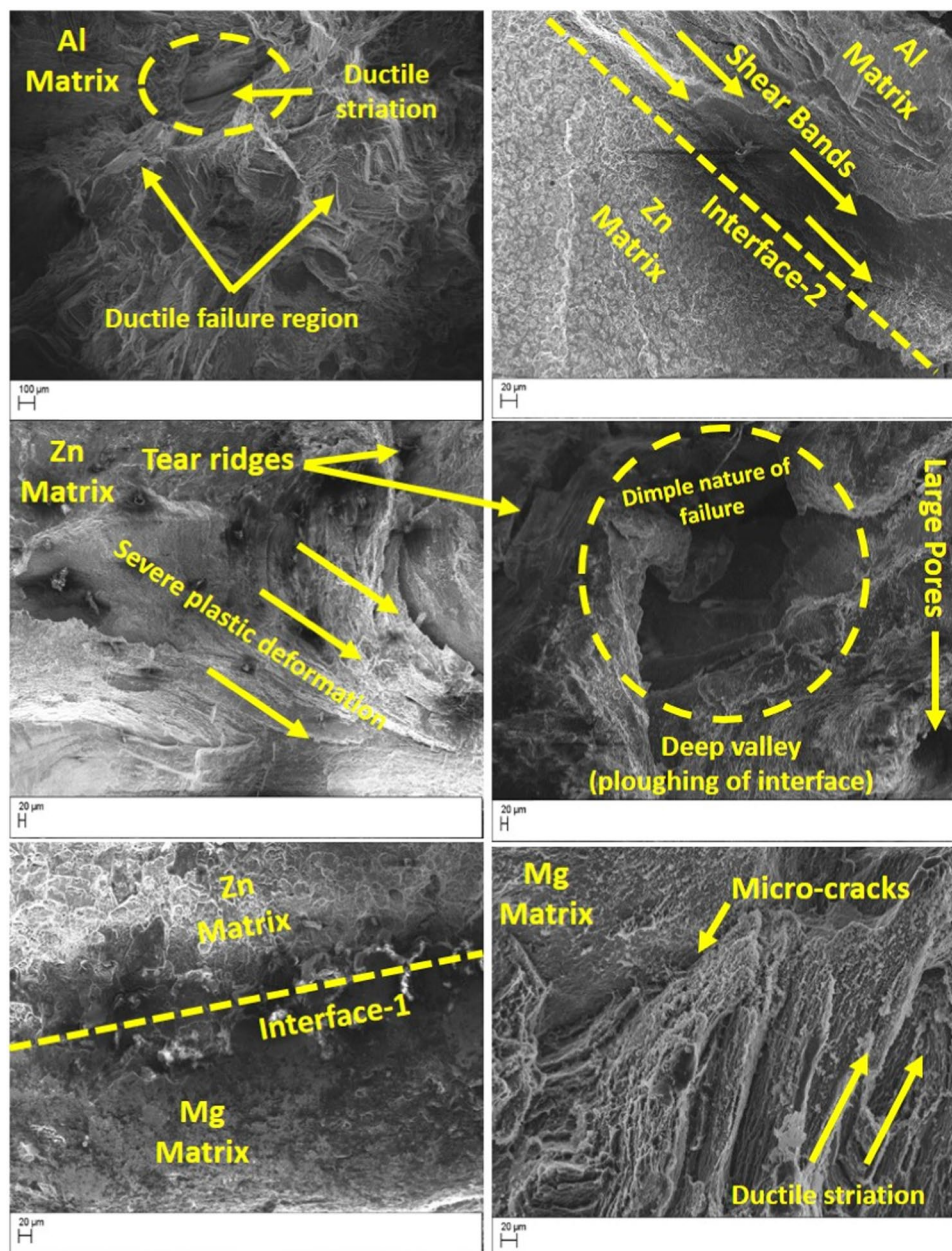
regions. This shows that the tensile force is equally distributed to all three matrix materials and their interfaces due to the strong bonding and improved strengthening mechanism during FSP.

The corrosion rate (CR) of the developed specimen of AZ31B–Zn–Al 1100 laminated composite was studied through the weight loss method. The initial and final weights were measured using the weighing balance (make: MS205DU, Mettler Toledo). The density of the prepared FSAM sample was calculated through the weighing balance setup, which works on Archimedes's principle. The exposed surface area was 1.87 cm^2, which is shown in Fig. 2(h), and the test duration was 7 days. Further, the corrosion rate was

calculated and found as 0.891 mm/year or 0.00244 mm/day. The test result shows that the obtained CR is less than the previously reported studies and is also in line with the microstructural outcomes. Further, the 3D surface profiles of the prepared sample were taken before and after the test and presented in Fig. 10 (a–e). Figure 10 (a–c) shows the 3D profiles of the AZ31B (Fig. 10a), Zn (Fig. 10b), and Al1100 (Fig. 10c) laminated composites before the corrosion test.

During the corrosion test, the metal deteriorates in a salt solution which works as a corrosive environment for the sample. The material reacts with the salt solution and corrodes the outermost layer. However, the presence of passive oxide layers, fine microstructures, and material density plays
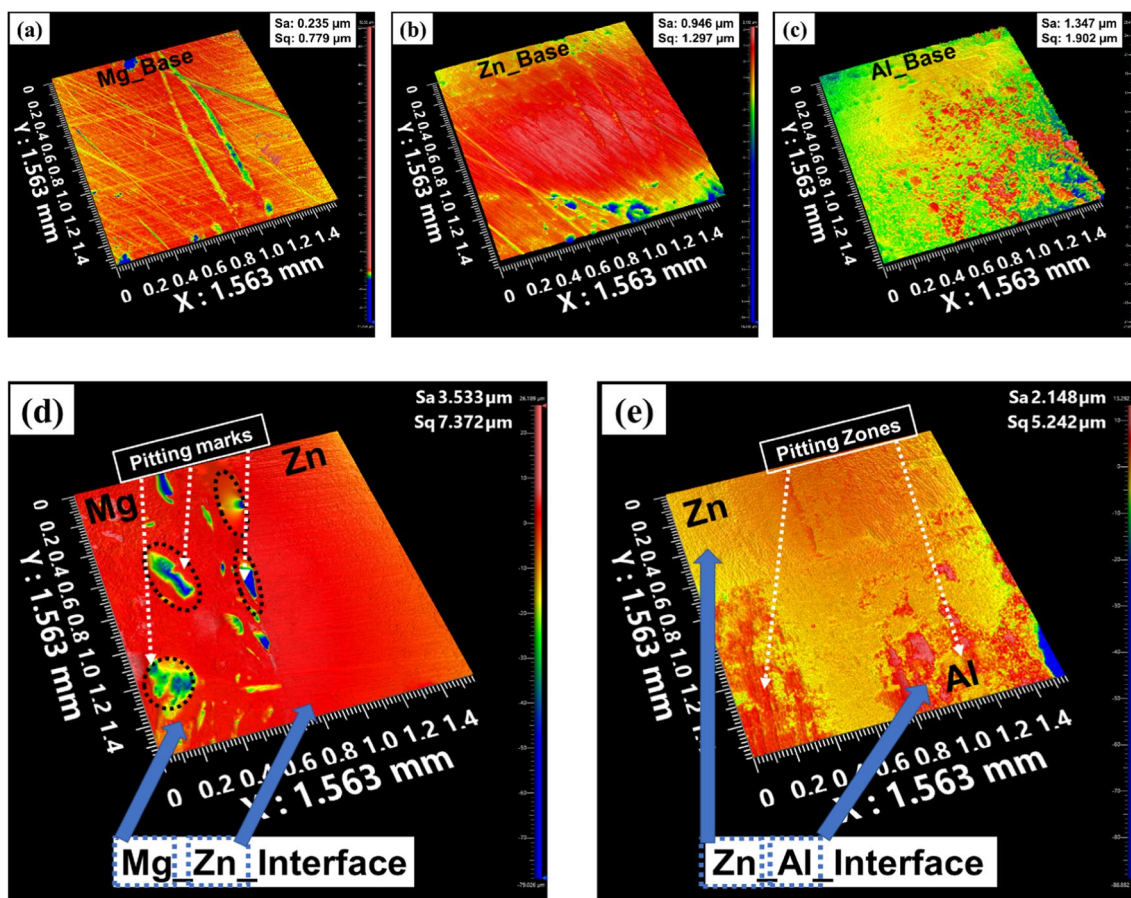
Fig. 10 The 3D profiles of the **a** AZ31B, **b** Zn, and **c** Al1100 before the corrosion sample, and **d** AZ31B–Zn interface and **e** Zn–Al1100 interface after the corrosion test

a vital role in preventing pitting in the corrosive environment [28]. In AZ31B–Zn–Al 1100 laminated composite specimen, the density of AZ31B is the lowest, followed by Al 1100 and Zn, respectively, which dictates that AZ31B has more probability to get corrodes in the salt solution. Moreover, Fig. 10(d) and (e) depicts the 3D profiles of the AZ31B–Zn and Zn–Al 1100 interface profiles. From the results, it can be seen that AZ31B and Al 1100 parts show more corrosion as compared to the Zn. The results dictate that AZ31B has more pitting as compared to Al 1100. Further, no such noticeable pitting was formed over the Zn layer, which works as a protecting layer between the AZ31B and Al 1100. The 3D profiles also dictate the change in the surface roughness values at both interfaces. The AZ31B–Zn interface shows higher S_a (3.533 μm) and S_q (7.372 μm) values compared to the Zn–Al 1100 (S_a: 2.148 μm, S_q: 5.242 μm) interface, which supports the results of the pitting phenomena of AZ31B–Zn–Al 1100 laminated composite.

Friction, which happens when matting parts scour against one another during operation, is widely examined in parts like the power trains in automobiles. Friction causes heat

and wears in these regions. Most mechanical system failures are brought on by heat generation and wear brought on by friction, resulting in large financial losses [28]. Figure 11 shows the tribological test results to examine parts and the material properties to minimize such losses. It shows the variation of the coefficient of friction against the test time for the interfaces (AZ31B–Zn and Zn–Al 1100) and base materials (AZ31B, Zn, and Al 1100). During the test, when the counter ball comes into contact with the specimen, the coefficient of friction increases linearly for a short period, which can be explained by the stick-slip phenomenon. Further wear takes place, and the friction coefficient reaches a maximum value, and then it becomes stable. The average value of the coefficient of friction of the laminated composite sample was observed to be 0.4127, 0.2187, and 0.5237 for Al, Mg, and Zn, respectively, which is lower than that of their base metal. In contrast, the average COF at the interface of Mg–Zn is 0.212, which is less than that of individual Mg and Zn COF values. Similarly, the COF value at the interface of Al–Zn is 0.3098, which is less than that of individual Al and Zn. From the above result, it can be concluded that there was

Fig. 11 **a** COF with time at different locations and **b** average COF of AZ31B–Zn–Al 1100 laminated composite and pure material specimens
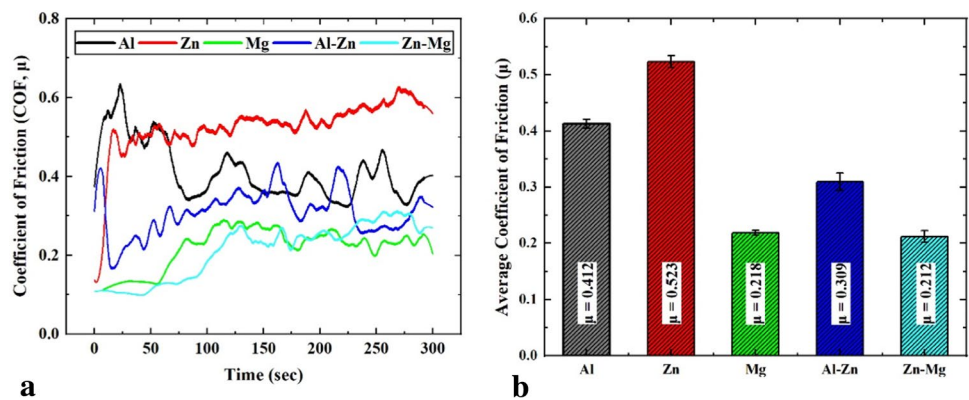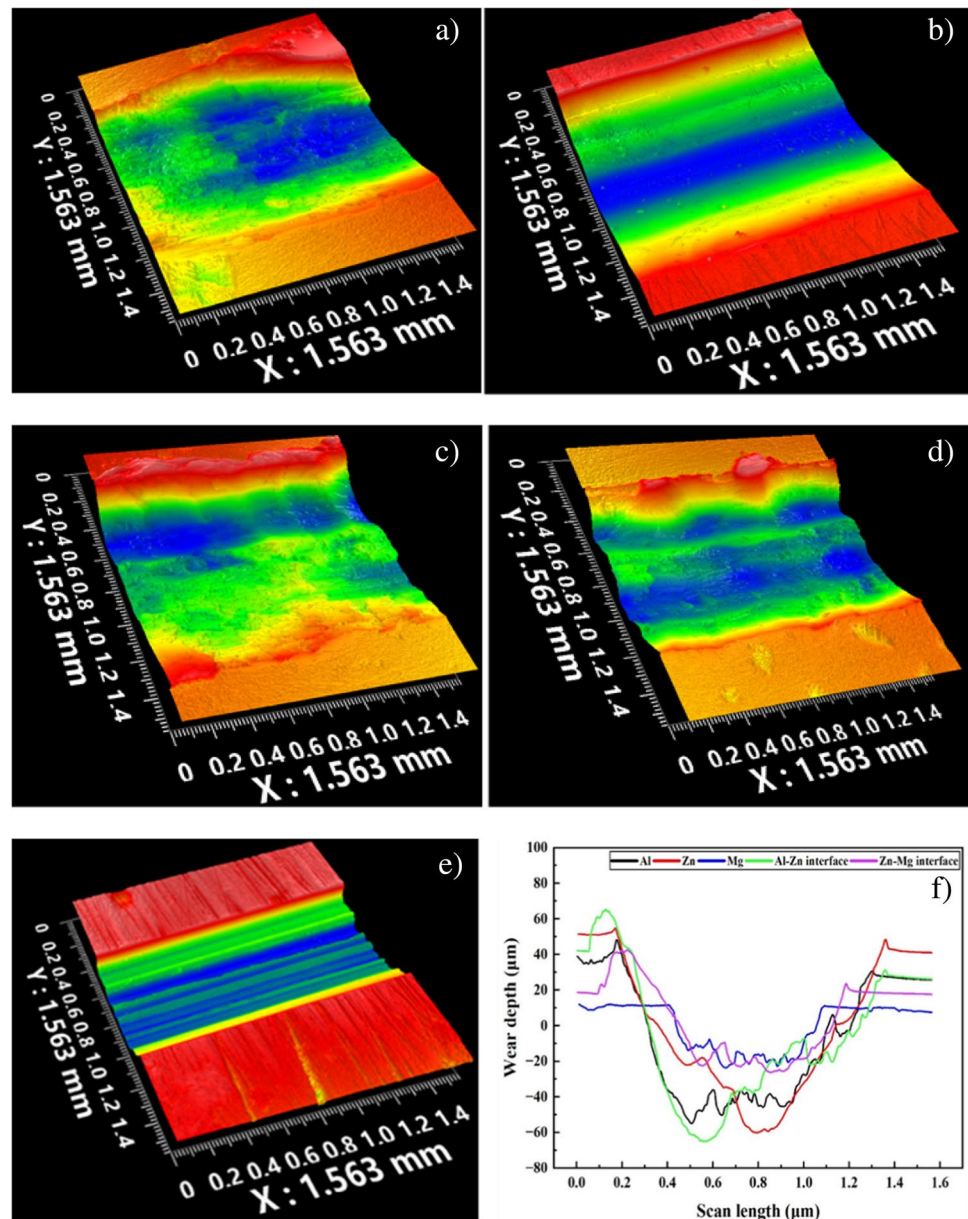

intermixing of material at the interface, so the COF value is lying between two alloys at the interface. Maximum COF was encountered for Zn alloys and minimum at the interface of Zn–Mg. The improvement in tribological performance may be attributed to grain size refinement due to intense plastic deformation and dynamic recrystallization, which leads to an increment in hardness value and, thus, the coefficient of friction decreases. The lower friction coefficient of the laminated composite sample may also be attributed to the decrement in adhesive and abrasive wear due to the higher hardness of the laminated composite part [41–45].

Furthermore, a non-contact-type 3D profilometer (model: Zygo, Ametek Newview-9000) was used to analyze the surface topography of the wear tracks formed on the laminated composite specimen. Crater dimensions were measured at five different locations: base AZ31B, Zn, and Al 1100 and at the interface of AZ31B–Zn and Zn–Al 1100. Figure 12 represents the 3D profile of the wear track and corresponding cross-sectional profile for the AZ31B–Zn–Al 1100 laminated composite. Fluctuation in the depth of the wear track at all locations can be observed due to the entrapment of the wear debris in the wear track [46]. Therefore, the average crater depth and width value have been calculated by taking five different slices for each location. The average cavity depths of wear track at Al 1100, Zn, AZ31B, Al 1100–Zn interface, and AZ31B–Zn interface were found to be 103.11 μm, 117.96 μm, 37.088 μm, 130.21 μm, and 68.53 μm, respectively. Similarly, average wear widths were observed to be 1.12 mm, 1.21 mm, 0.67 mm, 1.22 mm, and 0.964 mm, respectively, for such locations.

4 Conclusion

The laminated composite AZ31B–Zn–Al 1100 is built up efficiently through the friction stir additive manufacturing (FSAM) technique. The microstructural features of the developed composite show the improvement in grain structure at both the interfaces of the dissimilar materials. The overall crystallographic structure is fine oriented from advancing to retreating side through equiaxed and refined grains with a large number of grain boundaries. The average grain size of 6.29 μm at the AZ31B–Zn interface and 1.21 μm at the Zn–Al 1100 interface is confirmed by the EBSD results. Due to the grain refinement and microstructural modification technique of FSAM, the overall mechanical properties are improved. The laminated composite's tensile strength is 171.5 MPa at 15.5% elongation. Microhardness is found in varying natures and an improved manner while measuring from the cross-section of the built-up composite. The maximum microhardness is reported as 105 HV at the interface of AZ31B–Zn and 84.6 HV at the interface of Zn–Al 1100. The overall results of the FSAM route suggest it applies to a process where the improved mechanical properties of the dissimilar layers are the key requirement. The corrosion study revealed a corrosion rate of 0.891 mm/year or 0.00244 mm/day. AZ31B and Al 1100 parts show more corrosion than the Zn. The average COF at the interface of Mg–Zn is 0.212, and at the interface of Al–Zn is 0.3098, which is less than that of individual Mg, Al, and Zn. The average cavity depths of wear track at Al 1100, Zn, AZ31B, Al 1100–Zn interface, and AZ31B-Zn interface were found to be 103.11 μm, 117.96 μm, 37.088 μm, 130.21 μm, and 68.53 μm, respectively. As a future prospect, the proposed FSAM method can be an alternative to process magnesium efficiently and can provide the solution for many biomedical engineering.

Fig. 12 Wear track 3D plot of **a** Al 1100, **b** Al 1100–Zn interface, **c** Zn, **d** Zn–AZ31B interface, **e** AZ31B, and **f** cross-section profile of the wear track

Declarations

Ethics approval The research does not involve human participants or animals and the authors warrant that the paper fulfills the ethical standards of the journal.

Consent to participate It is confirmed that all the authors are aware and satisfied of the authorship order and correspondence of the paper.

Consent for publication All the authors are satisfied that the last revised version of the paper is published without any change.

Competing interests The authors declare no competing interests.

References

1. Wong KV, Hernandez A (2012) A review of additive manufacturing. ISRN Mech Eng 1:1–10

2. Elyasi M, Razaghian A, Moharami A, Emamy M (2023) Effects of multi-pass friction stir processing on mechanical and tribological properties of Mg–Zn–Zr alloys. J Mater Res Technol 24:4730–4742. https://doi.org/10.1016/j.jmrt.2023.04.104

3. Srivastava AK, Kumar N, Dixit AR (2021) Friction stir additive manufacturing–an innovative tool to enhance mechanical and microstructural properties. Mater Sci Eng B 263:114832

4. Elyasi M, Razaghian A, Moharami A, Emamy M (2022) Effect of zirconium micro-addition and multi-pass friction stir processing on microstructure and tensile properties of Mg–Zn–Si alloys. J Mater Res Technol 20:4269–4282. https://doi.org/10.1016/j.jmrt.2022.08.155

5. Srivastava AK, Saxena A, Dixit AR (2021) Investigation on the thermal behaviour of AZ31B/waste eggshell surface composites produced by friction stir processing. Compos Commun 28:100912

6. Kumar N, Bhavsar H, Mahesh PVS et al (2022) Wire arc additive manufacturing–a revolutionary method in additive manufacturing. Mater Chem Phys 285:126144

7. Nguyen N, Park JG, Zhang S, Liang R (2018) Recent advances on 3D printing technique for thermal-related applications. Adv Eng Mater 20:1700876

8. Vidakis N, Petousis M, Mountakis N et al (2022) Material extrusion 3D printing and friction stir welding: an insight into the weldability of polylactic acid plates based on a full factorial design. Int J Adv Manuf Technol 121:3817–3839. https://doi.org/10.1007/s00170-022-09595-19

9. Li L, Post B, Kunc V et al (2017) Additive manufacturing of near-net-shape bonded magnets: prospects and challenges. Scr Mater 135:100–104

10. Sinmazçelik T, Avcu E, Bora MÖ, Çoban O (2011) A review: fibre metal laminates, background, bonding types and applied test methods. Mater Des 32:3671–3685

11. Ngo TD, Kashani A, Imbalzano G et al (2018) Additive manufacturing (3D printing): a review of materials, methods, applications and challenges. Compos B Eng 143:172–196

12. Hangai Y, Masuda A, Suzuki R et al (2023) Easy dismantling and separation of friction stir-welded steel and aluminum by foaming. Int J Adv Manuf Technol 126:561–568. https://doi.org/10.1007/s00170-023-11139-0

13. Teng L, Lu X, Luan Y, Sun S (2023) Predicting axial force in friction stir welding thick 2219 aluminum alloy plate. Int J Adv Manuf Technol 126:1025–1034. https://doi.org/10.1007/s00170-023-11175-w

14. Yan F, Li Q, Fu X et al (2023) Quality prediction of friction stir welded joint based on multiple regression: entropy generation analysis. Int J Adv Manuf Technol 125:5163–5183. https://doi.org/10.1007/s00170-023-10979-0

15. Moharami A, Razaghian A, Babaei B et al (2020) Role of Mg2Si particles on mechanical, wear, and corrosion behaviors of friction stir welding of AA6061-T6 and Al-Mg2Si composite. J Compos Mater 54:4035–4057. https://doi.org/10.1177/0021998320925528

16. Tabasi M, Farahani M, Givi MKB et al (2016) Dissimilar friction stir welding of 7075 aluminum alloy to AZ31 magnesium alloy using SiC nanoparticles. Int J Adv Manuf Technol 86:705–715. https://doi.org/10.1007/s00170-015-8211-y

17. Joshi SS, Patil SM, Mazumder S et al (2022) Additive friction stir deposition of AZ31B magnesium alloy. Journal of Magnesium and Alloys 10:2404–2420. https://doi.org/10.1016/j.jma.2022.03.011

18. Badkoobeh F, Mostaan H, Rafiei M et al (2023) Additive manufacturing of biodegradable magnesium-based materials: design strategies, properties, and biomedical applications. J Magnes Alloy 11:801–839. https://doi.org/10.1016/j.jma.2022.12.001

19. Mishra RS, Haridas RS, Agrawal P (2022) Friction stir-based additive manufacturing. Sci Technol Weld Join 27:141–165

20. Heidarzadeh A, Mironov S, Kaibyshev R et al (2021) Friction stir welding/processing of metals and alloys: a comprehensive review on microstructural evolution. Prog Mater Sci 117:100752. https://doi.org/10.1016/j.pmatsci.2020.100752

21. Staiger MP, Pietak AM, Huadmai J, Dias G (2006) Magnesium and its alloys as orthopedic biomaterials: a review. Biomaterials 27:1728–1734

22. Derazkola HA, Khodabakhshi F, Simchi A (2020) Evaluation of a polymer-steel laminated sheet composite structure produced by friction stir additive manufacturing (FSAM) technology. Polym Test 90:106690

23. Mukhopadhyay A, Saha P (2020) Mechanical and microstructural characterization of aluminium powder deposit made by friction stir based additive manufacturing. J Mater Process Technol 281:116648

24. Palanivel S, Nelaturu P, Glass B, Mishra RS (2015) Friction stir additive manufacturing for high structural performance through microstructural control in an Mg based WE43 alloy. Mater Des 1980-2015(65):934–952

25. Ho Y-H, Man K, Joshi SS et al (2020) In-vitro biomineralization and biocompatibility of friction stir additively manufactured AZ31B magnesium alloy-hydroxyapatite composites. Bioact Mater 5:891–901

26. Ho Y-H, Joshi SS, Wu T-C et al (2020) In-vitro bio-corrosion behavior of friction stir additively manufactured AZ31B magnesium alloy-hydroxyapatite composites. Mater Sci Eng C 109:110632

27. Martin LP, Luccitti A, Walluk M (2022) Repair of aluminum 6061 plate by additive friction stir deposition. Int J Adv Manuf Technol 118:759–773. https://doi.org/10.1007/s00170-021-07953-z

28. Rathi VR, Nirmal SD, Kokate SJ (2010) Corrosion study of mild steel, tor steel and CRS steel by weight loss method. J Chem Pharm Res 2(2):97–100 ISSN No: 0975-7384

29. Paidar M, Tahani K, Vaira Vignesh R et al (2020) Modified friction stir clinching of 2024-T3 to 6061-T6 aluminium alloy: effect of dwell time and precipitation-hardening heat treatment. Mater Sci Eng A 791:139734. https://doi.org/10.1016/j.msea.2020.139734

30. Moharrami A, Razaghian A, Paidar M et al (2020) Enhancing the mechanical and tribological properties of Mg2Si-rich aluminum alloys by multi-pass friction stir processing. Mater Chem Phys 250:123066. https://doi.org/10.1016/j.matchemphys.2020.123066

31. Prabhakar DAP, Shettigar AK, Herbert MA et al (2022) A comprehensive review of friction stir techniques in structural materials and alloys: challenges and trends. J Mater Res Technol 20:3025–3060. https://doi.org/10.1016/j.jmrt.2022.08.034

32. Srivastava AK, Dixit AR, Maurya M et al (2021) 20th century uninterrupted growth in friction stir processing of lightweight composites and alloys. Mater Chem Phys 266:124572

33. Srivastava AK, Nag A, Dwivedi S et al (2023) Effect of eggshell powder on the microstructural and thermal behaviour of Al7075/waste eggshell surface composites produced by solid-state friction stir processing developed for potential thermal applications. Int J Adv Manuf Technol 127:1243–1261. https://doi.org/10.1007/s00170-023-11600-0

34. Chaudhary B, Jain NK, Murugesan J (2022) Experimental investigation and parametric optimization of friction stir powder additive manufacturing process for aerospace-grade Al alloy. Int J Adv Manuf Technol 123:603–625. https://doi.org/10.1007/s00170-022-10211-5

35. Yuqing M, Liming K, Chunping H et al (2016) Formation characteristic, microstructure, and mechanical performances of aluminum-based components by friction stir additive manufacturing. Int J Adv Manuf Technol 83:1637–1647. https://doi.org/10.1007/s00170-015-7695-9

36. Rajawat MS, Pagrut S, Dwivedi S, Raj R, Dixit AR (2022) Microstructural characterization of friction stir assisted laminated lap welding of AA6063 sheets. Mater Today: Proc 56:949–953

37. Rath L, Kallien Z, Roos A et al (2023) Anisotropy and mechanical properties of dissimilar Al additive manufactured structures generated by multilayer friction surfacing. Int J Adv Manuf Technol 125:2091–2102. https://doi.org/10.1007/s00170-022-10685-3

38. Zhang Z, Tan ZJ, Li JY et al (2019) Experimental and numerical studies of re-stirring and re-heating effects on mechanical properties in friction stir additive manufacturing. Int J Adv Manuf Technol 104:767–784. https://doi.org/10.1007/s00170-019-03917-6

39. Hong X, Xiao G, Zhang Y, Zhou J (2021) Research on gradient additive remanufacturing of ultra-large hot forging die based on automatic wire arc additive manufacturing technology. Int J Adv Manuf Technol 116:2243–2254. https://doi.org/10.1007/s00170-021-07424-5

40. Zhao Z, Yang X, Li S, Li D (2019) Interfacial bonding features of friction stir additive manufactured build for 2195-T8 aluminum-lithium alloy. J Manuf Process 38:396–410

41. Moharrami A, Razaghian A, Emamy M, Taghiabadi R (2019) Effect of tool pin profile on the microstructure and tribological properties of friction stir processed Al-20 wt% Mg2Si composite. J Tribol 141:122202. https://doi.org/10.1115/1.4044672

42. Srivastava AK, Dwivedi S, Nag A, Kumar D, Dixit AR, Hloch S (2023) Microstructural, mechanical and tribological performance of a magnesium alloy AZ31B/Si3N4/eggshell surface composite produced by solid-state multi-pass friction stir processing. Mater Chem Phys 301:127694

43. Moharami A (2020) Improving the dry sliding-wear resistance of as-cast Cu-10Sn-1P alloy through accumulative back extrusion (ABE) process. J Mater Res Technol 9:10091–10096. https://doi.org/10.1016/j.jmrt.2020.07.022

44. Moharami A, Qodosi P (2022) Enhanced dry sliding friction and wear behaviors of Mg–Mg2Si composites. Compos Commun 36:101365. https://doi.org/10.1016/j.coco.2022.101365

45. Moazami MR, Razaghian A, Moharami A et al (2022) Enhancing the elevated temperatures tribological properties of Al–Mg2Si composites by in-situ addition of Ti-based intermetallics and hot working. J Mater Res Technol 21:1381–1394. https://doi.org/10.1016/j.jmrt.2022.09.120

46. Srivastava AK, Dwivedi S, Saxena A, Kumar D, Dixit AR, Singh GK, Verma R (2022) Tribological characteristics of Al359/Si3N4/eggshell surface composite produced by friction stir processing. Coatings 12(9):1362